

Enhanced thermoelectric figure of merit of individual Si nanowires with ultralow contact resistances

0. Abstract

Low-dimensional silicon-based materials have shown a great potential for thermoelectric applications due to their enhanced figure of merit ZT and high technology compatibility. However, their implementation in real devices remains highly challenging due to the associated large contact resistances (thermal and electrical). Herein we demonstrate ultralow contact resistance silicon nanowires epitaxially grown on scalable devices with enhanced ZT . Temperature dependent figure of merit was fully determined for monolithically integrated individual silicon nanowires achieving a maximum value of $ZT = 0.2$ at 620 K. Sidewise, this work accounts for the first time nearly zero thermal and electrical contact resistances in monolithically integrated bottom-up nanowires.

1. Introduction

The thermoelectric effect (TE) allows converting heat into electricity and vice versa with a typical efficiency of 5-10%. The easy scalability, high stability and lack of mobile parts of thermoelectric generators (TEGs) make them ideal candidates for applications where unmanned, reliable operation is critical. Two paradigmatic examples are RTGs (Radioisotope Thermoelectric Generators) in space missions – which convert heat from a nuclear source to electricity – or thermal energy harvesting in industrial environments to power remote wireless sensor nodes [1]. The efficiency of a thermoelectric material increases with its thermoelectric figure of merit $ZT=S^2\sigma T/\kappa$, where S is the Seebeck coefficient, σ is the electrical conductivity, κ the thermal conductivity and T the absolute temperature. Nano structuration allows increasing ZT by decreasing κ , because of the increased phonon scattering at the boundaries of the material [2]. In particular, highly doped silicon constitutes an excellent platform to exploit this effect since despite having a high power factor $S^2\sigma$, it also has a high κ , leading to a too low ZT for its direct thermoelectric application (0.01 at 300 K) [3]. Moreover, there is a major interest in using silicon due to its high natural abundance and compatibility with microelectronics mainstream fabrication technologies [4]. Silicon nanowires (Si NWs) with diameters in the order of ~ 100 nm present a significantly reduced κ and can be currently obtained with controlled morphology, crystallinity and doping [5,6].

With the improved thermoelectric performance of Si NWs, the importance lays on designing and assembling functional devices able to host dense arrays. However, it is not easy to implement NWs in structures able to use their thermoelectric properties, as their limited length – constrained to the 10-100 μm range due to inherent characteristics of the fabrication processes – makes them highly susceptible to the adverse effects of electrical and thermal contact resistances [6]. While approaches based on horizontal, top-down definition of Si NWs can overcome contact issues, they only allow the growth of nanowires in layer by layer

process, with the scaling-up limited by the number of lithography steps [7–9]. Moreover, these methods often require embedding, which contributes to increasing the effective κ . Top-down definition of vertical nanowire arrays by wet or dry etching allows to extend the growth in the off-plane direction to typically tenths of μm , but needs additional steps for the formation of top contacts and embedding, with the corresponding deleterious effects for σ/κ [10–12]. The bottom-up approach employed by Fonseca and co. [13–15] tackles contact, embedding and scalability issues, allowing growth and integration of dense arrays of suspended NWs in arbitrarily deep micro-trenches of thermoelectric devices in a single CVD step. Moreover, these devices are able to naturally set up a temperature difference across the NWs when placed on top of hot surfaces exposed to air, generating useful power from waste heat [16,17], while results often reported in literature for micro-TEG devices usually force a temperature difference with a heater, making difficult to ascertain an enhanced thermal performance [10,11,15,18].

While there has been a fast development and reporting of novel low-dimensional TE materials, most works do not concern on their integration or in predicting their behaviour in scaled-up, efficient devices [19]. Typically, thermoelectric characterization of Si-based nanostructures deals with nanomaterials obtained by means that, so far, have not demonstrated an efficient micro-device integration scheme, easily up-scalable and free from contact/parallel resistances [18,20,21]. Apart from this non-representative thermoelectric characterization approach, another issue often arises when determining ZT from different samples, i.e. by combining interrelated properties such as σ and κ measured in different nanowires, which may have different doping levels or effective cross sections [22,23]. Likely, this methodology contributes to the large scattering in κ and ZT values reported so far, for which there is still not an agreed explanation and which have been referred as controversial [24].

In this work, we report the complete thermoelectric characterization (ZT) of p-type Si NWs epitaxially grown by a CVD bottom-up approach on silicon, which enables their direct integration and usage in functional micro-TEG devices [14,16,17,25]. Electrical (σ) and thermal (κ) conductivities were measured in the very same single nanowire by using the DC self-heating method [26,27]. The less sensitive Seebeck measurement was performed in equivalent nanowires arrays integrated in dedicated microdevices – faithfully representing their averaged behaviour in the final working TEG. The method employed for evaluating ZT intrinsically allowed the quantification of the electrical and thermal contact resistances while avoided misleading results due to contact or cross-section artefacts. Thus, the methodology presented herein will enable the ultimate goal of accurately optimizing the silicon-based thermoelectric materials for μTEG devices applied to heat recovery, self-powered sensors, etc. [28–30].

2. Experimental

Boron (B) doped bottom-up Si NWs were grown by means of the Vapour Liquid Solid (VLS) mechanism within a Chemical Vapour Deposition (CVD) reactor. The NWs were grown by a CVD-VLS approach as in the works of [15,31] and optimized for their integration in thermoelectric devices, described in detail in [32,33].

Gold nanoparticles (Au NPs) were employed as a catalyst for VLS - NW growth and were deposited in two fashions: i) galvanic displacement [34,35], which led to a highly dense NP pattern within micro-trenches of Seebeck characterization devices and ii) electrostatic colloid deposition [36], which led to lower densities and a high control of the diameter of the deposited Au NPs and was employed for the single NW σ and κ characterization devices. The steps, conditions and compositions of the organic and aqueous phases for the galvanic displacement were the same as those employed in [32], except that a micro-emulsion parameter of $R = 10$ and a dipping time of $t_{dip} = 10$ min were employed in order to achieve a homogeneous deposition within trenches [33]. For the electrostatic colloid deposition, the approach of [33,36] was employed, using a commercial suspension of citrate stabilized 80 nm Au colloids from Sigma Aldrich and poly-L-lysine 0.1% to promote adhesion. The use of a 5% hydrofluoric acid and sonication of the suspension prior to the electrostatic deposition was found to be necessary for preventing agglomeration of colloids.

The boron-doped, bottom-up, $\langle 111 \rangle$ -aligned Si NWs were grown in a CVD reactor First Nano EasyTube 3000. The following CVD conditions were employed, optimized for thermoelectric application and device integration of Si NWs: growth temperature of 900 K, growth pressure of 2.5 Torr, growth time of 75 min, hydrogen (H_2) flow of 1000 sccm, silane (SiH_4) flow of 150 sccm (10% in H_2), diborane (B_2H_6) flow of 50 sccm (1500 ppm in H_2) and hydrochloric acid (HCl) flow of 30 sccm (99.95% pure). A 5% hydrofluoric acid etch immediately before growth (max. 3 min between etch and loading) was found to be crucial for obtaining aligned NWs [32].

Two types of characterization platforms were employed: Seebeck (S) devices (intended for measuring S in dense NW arrays, Fig. 1A-B) and single NW devices (for measuring σ and κ of individual NWs, Fig. 1C-F). The micro-devices were fabricated in cleanroom facilities by means of series of photolithography, metal evaporation and wet and dry etching microfabrication steps [17]. Fabrication and architecture are described in detail in Supplementary Info sections 2 and 3. The electrically active Si layers of these devices were p-type, highly doped with boron (ensuring a good contact with the boron-doped grown Si NWs) and featured tungsten metal contacts on top (allowing measuring safely without dewetting / eutectic melting issues at temperatures as high as 900 K).

Thermoelectric characterization was carried by performing electrical measurements of open circuit voltage (V_{oc}) and resistance (R) of micro-devices containing single NWs or NW arrays, from room temperature to 620 K. Details of the approach and the set-up are given in Supplementary Information sections 2 (Seebeck coefficient S) and 3 (σ and κ). Electrical measurements were performed using Keithley 2300 source-meter. For the Seebeck measurements the devices were loaded within a Linkam HFS720 PB4 gas-tight heating stage in air with the lid closed. For σ and κ measurements the devices were loaded into a custom, heated probe stage in vacuum (10^{-2} - 10^{-3} mbar).

3. Results

3.1 Si NW growth and microstructural characterization

Dense arrays of boron doped Si NWs and single suspended NWs were grown and integrated within Si micro-trenches by means of a bottom-up approach (CVD-VLS) in the conditions described in previous works [32] and [33], as shown in Fig. 1. These settings were optimized for achieving a high ZT and enabling scalable integration in Si-based thermoelectric generators [16,17,33].

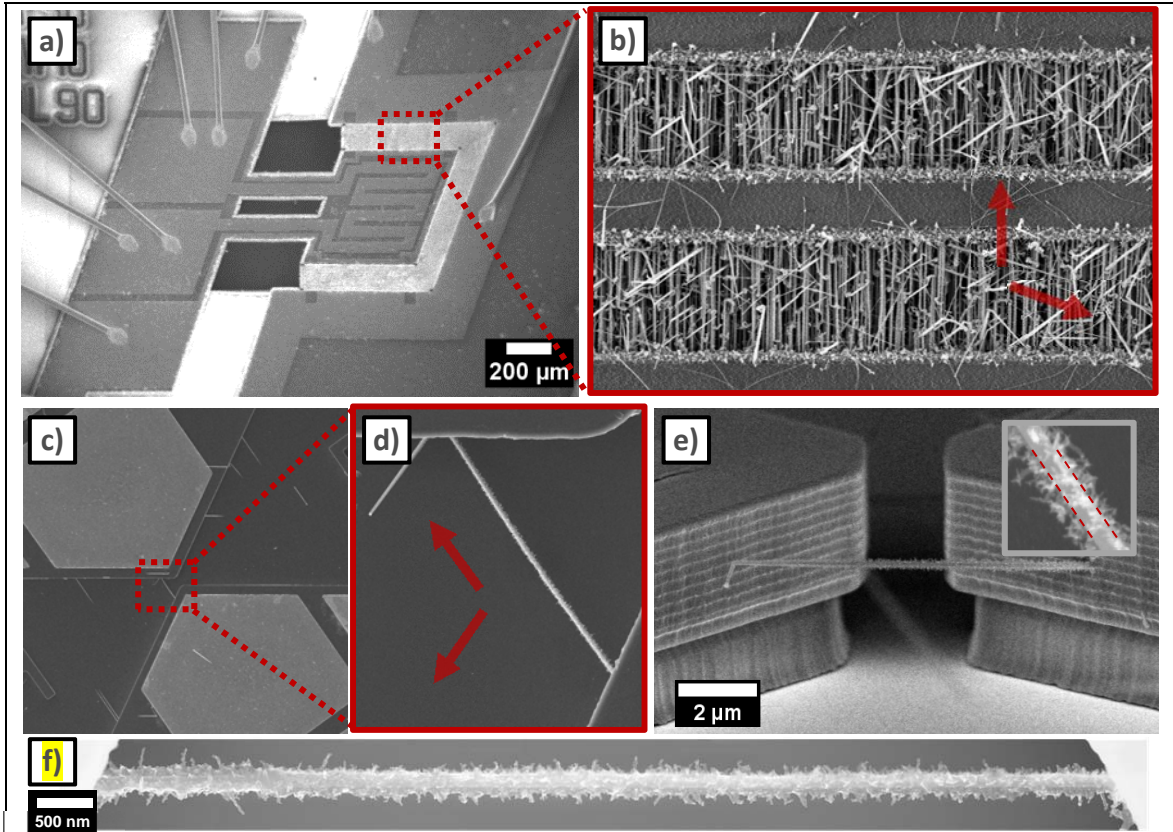


Fig. 1. Boron-doped Si NWs grown and integrated in micro-devices by means of bottom-up VLS approach. a, b) Seebeck characterization device, with dense arrays integrated in micro-trenches. c-e) σ and κ characterization device with a single suspended NW. The arrows in a) and d) indicate the $\langle 111 \rangle$ directions of the Si device layer. e) Tilted SEM image of a single NW suspended within a trench of a characterization device. The inset shows a higher magnification image used for the determination of the diameter (indicated with red dashed lines). f) Full-length SEM composed image of a single NW.

NWs grew epitaxially following the $\langle 111 \rangle$ directions of the Si of the trenches, allowing the integration of large number of NWs in parallel, with a density of $1\text{-}5\text{ NWs}/\mu\text{m}^2$ (Fig. 1A-B), or single nanowires between test devices (Fig. 1C-E). Thermodynamically favourable $\langle 111 \rangle$ growth direction for NWs was confirmed in a former study by TEM diffraction [32,37]. In the present work, SEM images obtained from top confirmed the epitaxial nature of the growth, showing NWs aligned with the $\langle 111 \rangle$ directions of the device layer (Fig. 1B, Fig. 1D). The process time was long enough to make the nanowires connect at the opposite wall of the trenches while keeping the crystal continuity with the Si of the device (i.e. monolithically), which ensures low electrical and thermal contact resistances [15,38]. The formation of monolithic contacts is confirmed by the angle of 70.1° between the direction of the NW and that of the secondary segment observed Fig. 1D, which corresponds to the angle between two different directions of the $\{111\}$ family (e.g. 111 and -111) [38].

NWs present a core of 70-130 nm surrounded with 5-30 nm thick shell, with distinct morphology at the base and at the tip (FigSup. 1 and FigSup. 2). The core presents a small tapering of 2 nm/ μm which allows for growth of NWs larger than 10 μm suitable for device integration. The structures surrounding the core are likely to be grown by direct vapour-solid growth, stemming from gold that migrated from the catalyst tip to the sidewalls. Some extent of gold migration is expected at the conditions employed in the in the present work, i.e. a relatively high temperature, low SiH_4 partial pressure and high boron concentration, for VLS standards using Au + SiH_4 [39]. This mechanism would explain the gradual evolution of the shell shape along the length of the NWs. More details about the growth and the morphology of the NWs can be found in Supplementary Information section 1.

3.2 Thermoelectric characterization

3.2.1 Seebeck coefficient

Dense arrays of $\langle 111 \rangle$ Si NWs were integrated in micro-trenches of devices designed for measuring their Seebeck coefficient (Fig. 1A-B). These devices allow forcing and measuring a ΔT along the NWs by means of a micro-heater placed on top of a suspended platform, while measuring the generated open circuit voltage (V_{oc}). The V_{oc} vs. T curves presented clearly linear trends, which allowed to extract the Seebeck coefficient ($S = \Delta V / \Delta T$) as the slope of the corresponding linear fitting FigSup. 5. Additional details of the device, setup and approach are given in Supplementary Information section 2.

Fig. 2 shows the obtained Seebeck coefficient S as a function of temperature, compared to results from other works for B doped bulk Si [3,40–42] and for B doped Si NWs [42].

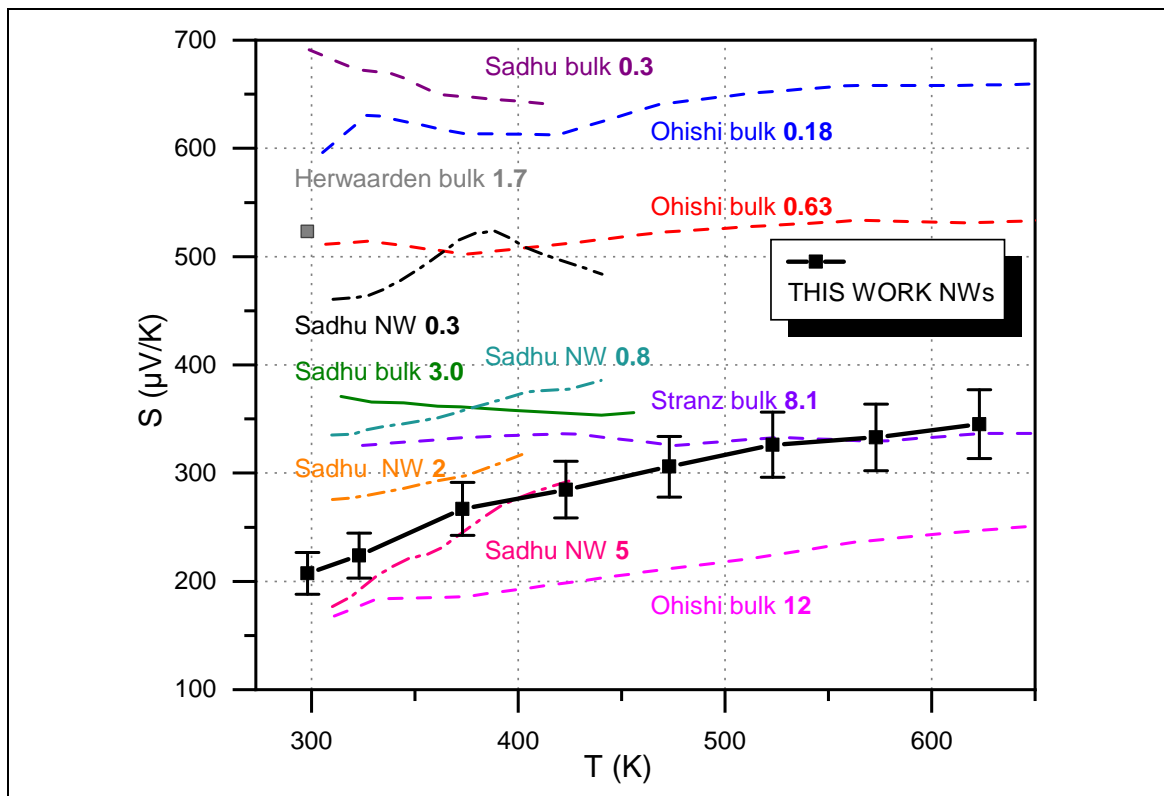


Fig. 2. Seebeck coefficient S vs. temperature T measured in this work for bottom-up integrated, B doped Si NWs (connected black dots) and from references for B doped bulk Si (dashed lines [3,40–42]) and for

B doped Si NWs (dashed-dot lines [42]). The labels indicate the first author and the doping level in that work, in units of 10^{19} B atoms/cm³.

S increases from 200 to 345 $\mu\text{V}/\text{K}$ as T increases from 300 to 673 K. This steepness in T is not observed in highly doped bulk Si (10^{18} - 10^{20} cm⁻³) [3,40–42]. However, this trend is in agreement with the results obtained by Sadhu et al. for top-down Si NWs with high B doping. Thus, in the present NWs, the increasing trend is also associated to the diffusive term of the Seebeck coefficient, with the phonon drag one suppressed due to a drastic scattering of longest-wavelength, electron-interacting phonons at the boundaries [42].

Observing the tendency at low T – between the values of [42] for NWs with a doping of 2 and $5 \cdot 10^{19}$ cm⁻³ – and the stabilization at 623 K – between the bulk values of [42] for $3 \cdot 10^{19}$ cm⁻³ and of [40] for $8.1 \cdot 10^{19}$ cm⁻³ – an approximated doping level of $2.5 \cdot 10^{19}$ cm⁻³ is estimated for the bottom-up, B doped Si NWs obtained in this work.

3.2.2 Electrical and thermal measurements

Bottom-up, B-doped, <111>-aligned Si NWs were grown and integrated in single suspended NW devices (Fig. 1C-F). The direct current (DC) self-heating method was used to measure each one of the nanowires [26]. Three NWs with a length close to the micro-trenches gap (i.e. 15 μm) were measured in vacuum at different temperatures within the range 300-620 K. This procedure allows to simultaneously measure the electrical and thermal conductivity of a NW, preventing potential errors due to differences between samples or evolution with time. More details of the measurement and the employed devices are given in the Supplementary Information section 3.

The κ values at 300 K are plotted in Fig. 3A with respect the NW diameter, together with analogous reference results for smooth NWs – grown by isotropic etching or VLS [5,27,43] – and for rough NWs – grown by wet etching [44]. Fig. 3B shows which doping level can be inferred when comparing the average values of σ and the temperature coefficient of the electrical resistance (TCR) at 300 K obtained herein with reference data.

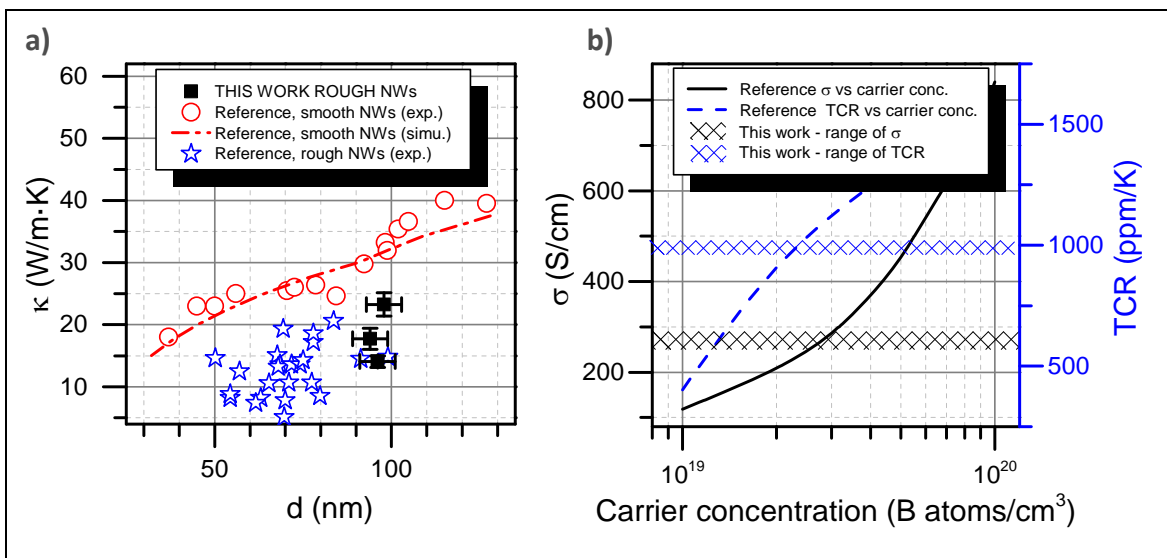


Fig. 3. a) thermal conductivity κ of the measured NWs (black squares) with respect to diameter d , along with reference data (experimental values for smooth NWs: [5,27,44], simulation for smooth NWs [45] and experimental values for rough NWs [44]). b) reference data for σ [46] and TCR [47,48] vs. doping

level in boron-doped bulk Si. The shaded areas indicate the average values measured in the present work.

The room temperature average σ value (~ 270 S/cm) corresponds to a boron doped Si bulk with a doping level of $2\text{-}3 \cdot 10^{19}$ cm $^{-3}$, as inferred by comparing with experimental data from [46] (Fig. 3B). The TCR obtained at room temperature (~ 930 ppm/K) is in agreement with the model of [47,48] for Boron doped $\langle 111 \rangle$ bulk Si with an impurity concentration of $2\text{-}3 \cdot 10^{19}$ cm $^{-3}$. These results confirm the doping level of $2\text{-}5 \cdot 10^{19}$ estimated with the S measurements, and suggest that σ is not significantly affected by a potential increase of electron scattering or carrier depletion at the surface in the present, highly doped rough NWs [6].

Regarding κ , an average value of 18.3 ± 4.6 W/m K measured at room temperature was obtained for the NWs measured in this work, with diameters ranging 90-100 nm. This value is three to four times lower than in highly doped bulk [3] and is mainly attributed to increased phonon scattering at NW boundaries [5]. Moreover, the NWs have a κ below that expected from a totally diffusive phonon boundary scattering in intrinsic silicon – indicated by the smooth NW reference trend (red dots and line in Fig. 3A). Nevertheless, our values are consistent with those previously reported for rough NWs [44]. Surface roughness arising from the naturally appearing shell in the here fabricated NWs can be behind this behaviour (see Supplementary Information section 1), as well as the increased phonon-ionized impurity scattering expected from the high doping level [3]. As σ is not so drastically affected as κ – due to the relatively short mean free path of electrons with respect to phonons – the present wires possess a higher σ/κ and ZT (discussed in following sections), confirming the suitability of the doped nanowires for thermoelectric applications.

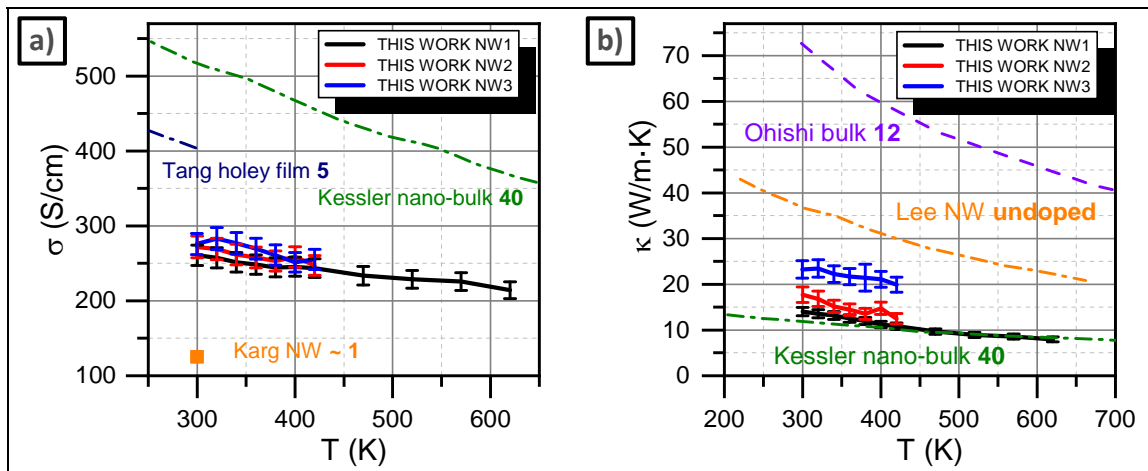


Fig. 4. Electrical conductivity (σ , in (a)) and thermal conductivity (κ , in (b)) of different nanowires with respect to temperature T , obtained by electrical measurements and the DC self-heating method. The error bars arise from the errors in the linear fittings of $\Delta R/\Delta P$ and $\Delta R_{I=0}/\Delta T$ (Supplementary Info 3) and the diameter estimation. References from other works reporting values for bulk (solid lines [3]) and nanostructures (dashed lines [43,49,50]) are included. The labels indicate the first author and the doping level in that work, in units of 10^{19} B atoms/cm 3 .

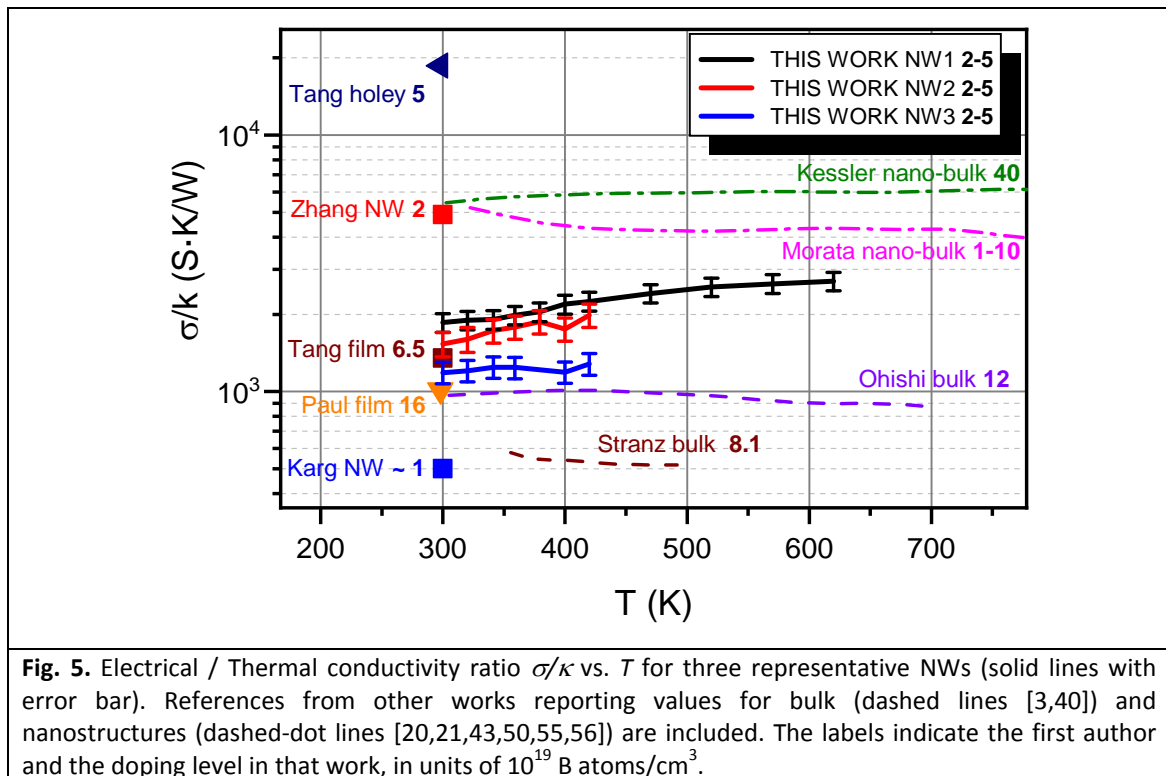
Fig. 4 shows σ and κ obtained for the measured NWs with respect to temperature of the measurement T . Both $1/\sigma$ and $1/\kappa$ increase linearly with T , as inferred from the plots of their respective resistances (see FigSup. 7). The linear increase of $1/\sigma$ with T is consistent with increasing phonon-electron scattering with increasing T in highly doped silicon, typical of

metals and highly doped semiconductors [51]. Analogously, the linear increase of $1/\kappa$ could be explained by increasing phonon-phonon Umklapp (anharmonic) scattering with increasing T , as one would expect for intrinsic bulk Si [52]. However, since boundary and impurity phonon scattering part are expected to dominate in this system – both increasing with increasing phonon frequency –, it is more likely that this trend is associated to a higher effectivity of these mechanisms at higher T , because of the higher population of high frequency modes [53,54].

3.2.3 σ/κ ratio

The relation σ/κ is proportional to ZT and representative of the effectivity of nanostructuration-derived enhancement of the thermoelectric efficiency. This ratio can be calculated directly from the electrical and thermal resistances as $\sigma/\kappa = R_{th}/R_{l=0}$ and thus – differently from σ and κ – it is not affected by possible errors regarding diameter determination (Supplementary Info section 3).

Fig. 5 shows σ/κ vs. T of three NWs from 300 to 620 K, compared with other values obtained from the literature for doped Si bulk [3,40] and doped Si nanostructures of different types [20,21,43,50,55,56]. Only data from works in which it is ensured that σ and κ were obtained for the same sample are included, for the sake of comparison.



The σ/κ value for the here fabricated NWs is presented in Fig. 5. The values range from 1100 to 2000 S-K/W at 300 K. Along the 300-620 K, σ/κ values up to 2700 S-K/W were obtained, with a moderate increase and saturation of the trend vs. T . The σ/κ values for the integrated bottom-up Si NWs presented in this work are at least two times higher than any value reported for highly doped bulk Si, despite having a lower doping level ($2\text{-}5 \cdot 10^{19} \text{ cm}^{-3}$ as estimated from S measurements, vs. $8\text{-}12 \cdot 10^{19} \text{ cm}^{-3}$, from [3,40]). This increase of σ/κ confirms the positive effects of nanostructuration for the NWs obtained herein for thermoelectric

application, i.e. increased phonon vs. electron scattering. These results are in a good position when comparing with similarly doped Si bottom-up NWs [43] and Si thin [20,55], possibly because of the low contact resistance and the high surface roughness of the present NWs, compared to smoother structures [44]. While other works reported more complex Si nanomaterials with higher doping and higher σ/κ (nano-bulk from [50,56] and nano-holes from [20,57]), to our knowledge, the present one is the first to report on the characterization of a nanomaterial which can be directly grown and integrated within MEMS using mature and scalable techniques. Other structures with remarkable performance also obtained by MEMS-compatible procedures, like holey membranes, lack from a straightforward fabrication technique that allows to obtain them in suspended platforms [20], as is the case of the bottom-up NW arrays obtained in the present and related works [14–17,25,33].

3.2.4 Figure of merit ZT

Fig. 6 shows the thermoelectric figure of merit ZT of the B-doped, $\langle 111 \rangle$, bottom-up integrated Si NWs with respect to T , obtained with the data from Fig. 2 (S from an average of dense arrays) and Fig. 5 (σ/κ from three representative NWs). References from other works reporting the thermoelectric figure of merit of highly doped p-type Si and its nanostructures are included for comparison.

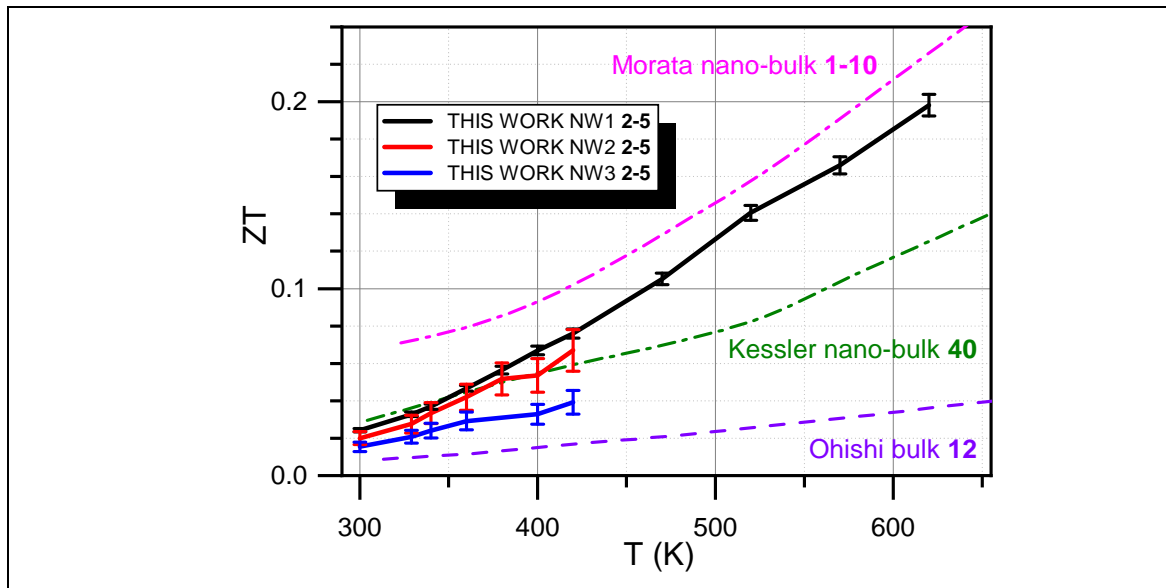


Fig. 6. Thermoelectric figure of merit ZT vs. T for three representative NWs (connected dots). References from other works reporting ZT vs T values for bulk (solid line [3]) and nanostructures (dashed lines [50,56]) are included. The labels indicate the first author and the doping level in that work, in units of 10^{19} B atoms/cm³.

All the NWs obtained in this work perform at least three times better than the highest doped p-type bulk Si [3]. Moreover, the average behaviour of the NWs equals and surpasses that of highly-doped nanostructure bulk of [50] and approaches that of [56] as T is increased. As discussed in the previous section, the more complex systems of [20,57] (ZT of 0.3-04, not included in Fig. 6) lack full scalability and co-integrability with MEMS devices.

The steep raise of ZT with T is expected to continue and is due to: i) the increasing S observed in Fig. 2, attributed to the diffusive contribution of the Seebeck S_e ; ii) the stabilization of σ/κ

observed in Fig. 5, which is likely to maintain if both the electrical and the thermal resistances keep their linear trends with T due to phonon-phonon and phonon-electron scattering; and iii) the high bandgap and doping level of Si, which implies that the Seebeck coefficient will not be negatively affected because the onset of the bipolar effect until higher $T \sim 1000$ K.

3.3 Contact resistances

The total resistance, electrical or thermal, of a single NW integrated in a device can be expressed as the sum of a length-dependent term proportional to L , a resistivity ($\rho = 1/\sigma$ or $1/\kappa$) and a length-independent contact term R_c . The contact resistance R_c is originated by dissimilarities in the electrical/thermal properties between the NW and the contacting structures and is inversely proportional to the cross section of the connection A , as intuitively expected. Thus, the quality of interfaces is represented by the contact resistivity ρ_c , defined as the constant given by $\rho_c = R_c \cdot A$, which is dependent on the two materials forming the interphase [58].

In thermoelectric devices – and specially in nanostructure-based ones, which generally feature a short length – the R_c term is particularly detrimental as it contributes to significantly increase the electrical resistance of the device (lowering effective σ) and to lower the ΔT experimented by the material (lowering generated voltage and thus effective S) [59,60].

A series of NWs with a wide range of lengths were grown and characterized in order to have statistically relevant data for determining thermal and electrical contact resistivity, using the transmission line method [61]. This allows to obtain ρ_c as half the intercept of an $R \cdot A$ vs L plot, where R is the resistance, A is the cross section and L is the length. More details are given in the Supplementary Information section 4. Fig. 7 shows the product of electrical ($R_{l=0}$) and thermal (R_{th}) resistance by A of the NWs with respect to L .

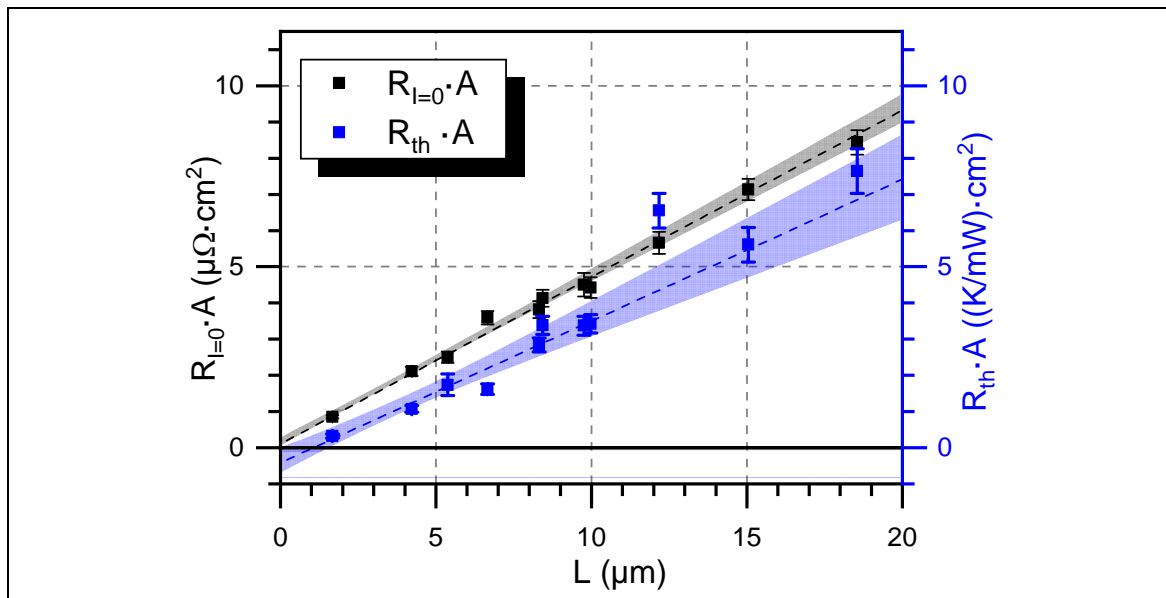


Fig. 7. Electrical ($R_{l=0}$) and thermal (R_{th}) resistances, multiplied by cross section A vs. length L for the Si NWs, at 300 K. Corresponding linear fittings and confidence bands of 95% are included.

Both electrical and thermal trends in Fig. 7 are clearly linear with intercepts close to zero, indicating a low effect of contact resistances. Measurements were performed from 300 to 380

K, yielding the electrical contact resistivity $\rho_{c,el}$ and the thermal contact resistivity $\rho_{c,th}$ with respect to T (FigSup. 9).

3.3.1 Electrical contact resistance

The system presents virtually-zero electrical contact resistance, showing $\rho_{c,el}$ of $0.05 \pm 0.02 \mu\Omega\cdot\text{cm}^2$, practically constant with T (FigSup. 9). It is worth to remark that this resistivity is much lower than that of Ti/Au contacts evaporated on top of Si NWs ($500 \mu\Omega\cdot\text{cm}^2$ [61]) or that of planar Ni-silicides evaporated on Si with a boron doping level similar to the one estimated for the present Si NWs ($0.1\text{-}0.7 \mu\Omega\cdot\text{cm}^2$ for a concentration of $2\text{-}5 \cdot 10^{19}\text{cm}^{-3}$ [62]). $\rho_{c,el}$ is also two orders of magnitude lower than the value firstly obtained by the same VLS growth/integration approach, also with $\text{SiH}_4/\text{B}_2\text{H}_6/\text{HCl}$ grown nanowires ($3\text{-}5 \mu\Omega\cdot\text{cm}^2$ [63]). This is likely because of: i) the increased doping level in the present work ($2\text{-}5 \cdot 10^{19}$ vs. $\sim 10^{18}$ in the former) and the location of the possible surface charges at the rough appendices – away from the core –, both contributing to avoid the formation of an important depletion region near the tip-contact region, as referred in [63]; and ii) the immediate loading of the sample within the CVD after the removal of native oxide of the trenches and the low base pressure employed, both contributing to avoid the formation of a perforated thin oxide layer which – despite not interfering with the crystalline quality of the connection – is surely decreasing the active area of the electrical contact [64]. The ultra-low $\rho_{c,el}$ value obtained herein allows for the NWs to be effectively used in micro-thermoelectric generators.

3.3.2 Thermal contact resistance

Regarding the thermal contact resistivity $\rho_{c,th}$, it is also very close to zero, with a negative value of $-0.21 \pm 0.08 \text{ (K/mW)}\cdot\text{cm}^2$ at room temperature (Fig. 7). Also, $\rho_{c,th}$ becomes more negative with increasing T (see FigSup. 9). Of course, a negative $\rho_{c,th}$ can only be an artefact arising from limitations of the measurement method. A plausible explanation can be the existence of a parallel heat transport mechanism that takes place only between relatively close ($\sim < 1 \mu\text{m}$) Si surfaces. This could be the case for near field radiative heat transport, which is expected to activate doped in Si at $T = 300\text{K}$ at a distance of $\sim 1 \mu\text{m}$. According to the work of Fu and Zhang for instance, the radiative heat flow between two highly doped Si plates at 300 and 400 K should increase swiftly at a distance of $3 \mu\text{m}$, multiplying by a factor 50-2000 as the distance is reduced from 100 to 10 nm [65]. Thus, one would expect that in the present work the $\sim 0.5 \mu\text{m}$ segments at NW edges are actually thermalized with the heat sinks. Therefore, thermal resistances equivalent to similar NWs $1 \mu\text{m}$ shorter are obtained. Indeed a shift of $\sim 1 \mu\text{m}$ to the left of the R_{th} curve in Fig. 7 would lead to the tendency expected for purely conductive transport, with a virtually null contact resistance. Moreover, the $\rho_{c,el}$ trend with T – more negative $\rho_{c,el}$ with increasing T (see FigSup. 9) – is in agreement with this explanation, as radiative transport – proportional to $T_2^4 - T_1^4$ – is expected to increase with overall T [26]. The anomalous R_{th} trend of the shortest wire with respect to T (not shown here) is likely to be explained by the same effect: a dominant, negative contact resistance term that grows with temperature and leads to the negative slope of R_{th} vs T for this particularly short NW ($1.7 \mu\text{m}$). It is worth mentioning that this negative $\rho_{c,th}$ effect is not universally appearing. For example, in the work of Raja et al. [27], positive value of $\sim 0.02 \text{ (K/mW)}\cdot\text{cm}^2$ was reported, likely because heat sinks of Ni were used, and thus a lower electromagnetic coupling was available for the near field radiative heat transport.

On the other hand, ignoring this effect and using $\kappa = L/R_{th} \cdot A$ leads to an apparent increase of κ with decreasing length, L , as appreciated in FigSup. 10. This explains why some κ values in FigSup. 10. are above the expected ones for the corresponding diameter (Fig. 3A). Thus, together with the dopant and roughness effects discussed with Fig. 3A, NW length surely adds some variability to the results obtained herein.

Due to the above discussed effect, the thermal contact resistivity of the bottom-up Si NWs monolithically integrated in Si heat sinks cannot be calculated by this – and possibly by any other – approach, in the range of interest for thermoelectric applications ($T > 300$ K). Moreover, since apparently this effect is inherent for NWs contacted in this way and cannot be avoided, these results can be regarded as a sort of length-dependent thermal conductivity as some authors do for ballistic transport [65] (with κ increasing – rather than decreasing – as $L \rightarrow 0$).

Nevertheless, it is worth to remark that, as seen in Fig. 7 and FigSup. 10. , the NWs with lengths ≥ 7 μm are clearly not affected by the contacts in a significant manner, implying that they can be readily used in μTEG devices as consistent thermoelements, with a high thermal-to-electrical resistance.

4. Conclusions

Boron doped $\langle 111 \rangle$ Si NWs with rough surface were grown and monolithically integrated in micro-fabricated test devices by means of the bottom-up CVD-VLS growth. Reliable figures of merit ZT of the NWs were obtained from thermal and electrical conductivities (σ and κ) simultaneously measured in the very same single NWs. The resulting ZT values raised swiftly from 0.015-0.02 at 300 K to 0.1-0.2 at 620 K, which represents a significant enhancement compared to highly doped bulk. A reduction of the thermal conductivity (κ) with respect to bulk and to smoother NWs, with an increased σ/κ ratio, corroborated the beneficial effect of nanostructuring. Finally, measurements of thermal and electrical resistances on a set of NWs with different geometries revealed ultra-low electrical and thermal contact resistances (<0.05 $\mu\Omega \cdot \text{cm}^2$ and <0.5 (K/mW) $\cdot \text{cm}^2$, respectively), which confirms for the first time that bottom-up nanowires NWs can be fully integrated, thus being excellent candidates as a thermoelectric material for μTEG devices.

Acknowledgements

This research was supported by the Generalitat de Catalunya-AGAUR (2017 SGR 1421) and by the Spanish Ministry of Economy and Competitiveness through the program ‘Retos de la Sociedad’ (TEC2016-78284-C3-1-R (AEI/FEDER, EU) MINAUTO & TEC2016-78284-C3-2-R (AEI/FEDER, EU) SIGNAL).

5. Bibliography

- [1] Champier D 2017 Thermoelectric generators: A review of applications *Energy Convers. Manag.*
- [2] Rowe D M 2006 *Thermoelectrics Handbook: Macro to Nano* (Boca Raton: CRC Press)

- [3] Ohishi Y, Xie J, Miyazaki Y, Aikebaier Y, Muta H, Kurosaki K, Yamanaka S, Uchida N and Tada T 2015 Thermoelectric properties of heavily boron- and phosphorus-doped silicon *Jpn. J. Appl. Phys.* **54**
- [4] Gadea G, Pacios M, Morata Á and Tarancón A 2018 Silicon-based nanostructures for integrated thermoelectric generators *J. Phys. D: Appl. Phys.* **51** 423001
- [5] Li D, Wu Y, Kim P, Shi L, Yang P and Majumdar A 2003 Thermal conductivity of individual silicon nanowires *Appl. Phys. Lett.* **83** 2934–6
- [6] Gadea G, Morata Á and Tarancón A 2018 Semiconductor Nanowires for Thermoelectric Generation pp 321–407
- [7] Ferri M, Suriano F, Roncaglia A, Solmi S, Cerofolini G F, Romano E and Narducci D 2011 Ultradense silicon nanowire arrays produced via top-down planar technology *Microelectron. Eng.* **88** 877–81
- [8] Totaro M, Bruschi P and Pennelli G 2012 Top down fabricated silicon nanowire networks for thermoelectric applications *Microelectron. Eng.*
- [9] Tomita M, Oba S, Himeda Y, Yamato R, Shima K, Kumada T, Xu M, Takezawa H, Mesaki K, Tsuda K, Hashimoto S, Zhan T, Zhang H, Kamakura Y, Suzuki Y, Inokawa H, Ikeda H, Matsukawa T, Matsuki T and Watanabe T 2018 Modeling, Simulation, Fabrication, and Characterization of a 10- μ W/cm² Class Si-Nanowire Thermoelectric Generator for IoT Applications *IEEE Trans. Electron Devices* **65** 5180–8
- [10] Xu B and Fobelets K 2014 Spin-on-doping for output power improvement of silicon nanowire array based thermoelectric power generators *J. Appl. Phys.* **115**
- [11] Curtin B M, Fang E W and Bowers J E 2012 Highly ordered vertical silicon nanowire array composite thin films for thermoelectric devices *J. Electron. Mater.* **41** 887–94
- [12] Buddharaju K, Singh N, Lo G Q, Lee S J and Li Y 2011 Chip-Level Thermoelectric Power Generators Based on High-Density Silicon Nanowire Array Prepared With Top-Down CMOS Technology *IEEE Electron Device Lett.*
- [13] Donmez Noyan I, Salleras M, Calaza C, Gadea G, Morata Á, Tarancón A and Fonseca L 2017 Improved thermal and electrical design for an all-Si thermoelectric micropower source *Proceedings of SPIE - The International Society for Optical Engineering* vol 10246, ed L Fonseca, M Prunnila and E Peiner p 102460Y
- [14] Donmez Noyan I, Salleras M, Calaza C, Santos J D, Gadea G, Morata Á, Dávila D, Tarancón A and Fonseca L 2015 Interdigitated design of a thermoelectric microgenerator based on silicon nanowire arrays *Proc. SPIE 9517, Smart Sensors, Actuators, and MEMS VII; and Cyber Physical Systems, 95172C* vol 9517, ed J L Sánchez-Rojas and R Brama p 95172C
- [15] Dávila D, Tarancón A, Calaza C, Salleras M, Fernández-Regúlez M, San Paulo A and Fonseca L 2012 Monolithically integrated thermoelectric energy harvester based on silicon nanowire arrays for powering micro/nanodevices *Nano Energy* **1** 812–9
- [16] Donmez Noyan I, Gadea G, Salleras M, Pacios M, Calaza C, Stranz A, Dolcet M, Morata Á, Tarancón A and Fonseca L 2019 SiGe nanowire arrays based thermoelectric microgenerator *Nano Energy* **57** 492–9

- [17] Donmez Noyan I, Dolcet M, Salleras M, Stranz A, Calaza C, Gadea G, Pacios M, Morata Á, Tarancón A and Fonseca L 2019 All-silicon thermoelectric micro/nanogenerator including a heat exchanger for harvesting applications *J. Power Sources* **413** 125–33
- [18] Li Y, Buddhharaju K, Tinh B C, Singh N and Lee S J 2012 Improved vertical silicon nanowire based thermoelectric power generator with polyimide filling *IEEE Electron Device Lett.* **33** 715–7
- [19] He R, Schierning G and Nielsch K 2018 Thermoelectric Devices: A Review of Devices, Architectures, and Contact Optimization *Adv. Mater. Technol.* **3** 1700256
- [20] Tang J, Wang H T, Lee D H, Fardy M, Huo Z, Russell T P and Yang P 2010 Holey silicon as an efficient thermoelectric material *Nano Lett.* **10** 4279–83
- [21] Zhang T, Wu S, Xu J, Zheng R and Cheng G 2015 High thermoelectric figure-of-merits from large-area porous silicon nanowire arrays *Nano Energy* **13** 433–41
- [22] Boukai A I, Bunimovich Y, Tahir-Kheli J, Yu J K, Goddard W A and Heath J R 2008 Silicon nanowires as efficient thermoelectric materials *Nature* **451** 168–71
- [23] Hochbaum A I, Chen R, Delgado R D, Liang W, Garnett E C, Najarian M, Majumdar A and Yang P 2008 Enhanced thermoelectric performance of rough silicon nanowires *Nature* **451** 163–7
- [24] Schierning G 2014 Silicon nanostructures for thermoelectric devices: A review of the current state of the art *Phys. Status Solidi A* **211** 1235–49
- [25] Fonseca L, Santos J D, Roncaglia A, Narducci D, Calaza C, Salleras M, Donmez Noyan I, Tarancón A, Morata Á, Gadea G, Belsito L and Zulian L 2016 Smart integration of silicon nanowire arrays in all-silicon thermoelectric micro-nanogenerators *Semicond. Sci. Technol.* **31** 084001
- [26] Völklein F, Reith H, Cornelius T W, Rauber M and Neumann R 2009 The experimental investigation of thermal conductivity and the Wiedemann-Franz law for single metallic nanowires *Nanotechnology*
- [27] Raja S N, Rhyner R, Vuttivorakulchai K, Luisier M and Poulidakos D 2016 Length Scale of Diffusive Phonon Transport in Suspended Thin Silicon Nanowires *Nano Lett.* [acs.nanolett.6b04050](https://doi.org/10.1021/acs.nanolett.6b04050)
- [28] Zhang D, Zhang K, Wang Y, Wang Y and Yang Y 2019 Thermoelectric effect induced electricity in stretchable graphene-polymer nanocomposites for ultrasensitive self-powered strain sensor system *Nano Energy*
- [29] Zhang D, Wang Y and Yang Y 2019 Design, Performance, and Application of Thermoelectric Nanogenerators *Small*
- [30] Yang Y, Pradel K C, Jing Q, Wu J M, Zhang F, Zhou Y, Zhang Y and Wang Z L 2012 Thermoelectric nanogenerators based on single Sb-doped ZnO micro/nanobelts *ACS Nano*
- [31] Islam M S, Sharma S, Kamins T I and Williams R S 2004 Ultrahigh-density silicon nanobridges formed between two vertical silicon surfaces *Nanotechnology* **15**
- [32] Gadea G, Morata Á, Santos J D, Dávila D, Calaza C, Salleras M, Fonseca L and Tarancón

- A 2015 Towards a full integration of vertically aligned silicon nanowires in MEMS using silane as a precursor *Nanotechnology* **26** 195302
- [33] Gadea G, Morata Á, Tarancón A, Santos J D and Pacios M 2017 *Integration of Si/Si-Ge nanostructures in micro-thermoelectric generators* (University of Barcelona)
- [34] Magagnin L, Bertani V, Cavallotti P L, Maboudian R and Carraro C 2002 Selective deposition of gold nanoclusters on silicon by a galvanic displacement process *Microelectronic Engineering*
- [35] Gao D, He R, Carraro C, Howe R T, Yang P and Maboudian R 2005 Selective growth of Si nanowire arrays via galvanic displacement processes in water-in-oil microemulsions *J. Am. Chem. Soc.*
- [36] Hochbaum A I, Fan R, He R and Yang P 2005 Controlled growth of Si nanowire arrays for device integration *Nano Lett.* **5** 457–60
- [37] Schmidt V, Senz S and Gösele U 2005 Diameter-dependent growth direction of epitaxial silicon nanowires *Nano Lett.* **5** 931–5
- [38] Islam M S, Sharma S, Kamins T I, Stanley Williams R and Williams R S 2005 A novel interconnection technique for manufacturing nanowire devices *Appl. Phys. A Mater. Sci. Process.* **80** 1133–40
- [39] Schmidt V, Wittemann J V. and Gösele U 2010 Growth, thermodynamics, and electrical properties of silicon nanowires *Chem. Rev.*
- [40] Stranz A, Kähler J, Waag A and Peiner E 2013 Thermoelectric properties of high-doped silicon from room temperature to 900 K *J. Electron. Mater.* **42** 2381–7
- [41] Van Herwaarden A W W 1984 The seebeck effect in silicon ICs *Sensors and Actuators* **6** 245–54
- [42] Sadhu J, Tian H, Ma J, Azeredo B, Kim J, Balasundaram K, Zhang C, Li X, Ferreira P M and Sinha S 2015 Quenched phonon drag in silicon nanowires reveals significant effect in the bulk at room temperature *Nano Lett.*
- [43] Karg S, Mensch P, Gotsmann B, Schmid H, Kanungo P Das, Ghoneim H, Schmidt V, Björk M T, Troncale V and Riel H 2013 Measurement of thermoelectric properties of single semiconductor nanowires *J. Electron. Mater.* **42** 2409–14
- [44] Lim J, Hippalgaonkar K, Andrews S C, Majumdar A and Yang P 2012 Quantifying surface roughness effects on phonon transport in silicon nanowires *Nano Lett.* **12** 2475–82
- [45] Mingo N, Yang L, Li D and Majumdar A 2003 Predicting the Thermal Conductivity of Si and Ge Nanowires *Nano Lett.* **3** 1713–6
- [46] Thurber W R 1980 Resistivity-Dopant Density Relationship for Boron-Doped Silicon *J. Electrochem. Soc.*
- [47] Klaassen D B M 1992 A unified mobility model for device simulation-I. Model equations and concentration dependence *Solid State Electron.*
- [48] Klaassen D B M 1992 A unified mobility model for device simulation-II. Temperature dependence of carrier mobility and lifetime *Solid State Electron.*

- [49] Park Y H, Kim J, Kim H, Kim I, Lee K-Y Y, Seo D, Choi H J and Kim W 2011 Thermal conductivity of VLS-grown rough Si nanowires with various surface roughnesses and diameters *Appl. Phys. A* **104** 7–14
- [50] Kessler V, Gautam D, Hülser T, Spree M, Theissmann R, Winterer M, Wiggers H, Schierning G and Schmechel R 2013 Thermoelectric properties of nanocrystalline silicon from a scaled-up synthesis plant *Adv. Eng. Mater.* **15** 379–85
- [51] Conwell E M 1967 *High Field Transport in Semiconductors* (Solid State Physics)
- [52] Mingo N 2003 Calculation of Si nanowire thermal conductivity using complete phonon dispersion relations *Phys. Rev. B - Condens. Matter Mater. Phys.*
- [53] Zou J and Balandin A 2001 Phonon heat conduction in a semiconductor nanowire *J. Appl. Phys.*
- [54] Maire J, Anufriev R and Nomura M 2017 Ballistic thermal transport in silicon nanowires *Sci. Rep.* **7**
- [55] Paul O, Arx M Von and Baltes H 1995 Process-dependent Thermophysical Properties Of CMOS IC Thin Films *Proc. Int. Solid-State Sensors Actuators Conf. - TRANSDUCERS '95*
- [56] Morata Á, Pacios M, Gadea G, Flox C, Cadavid D, Cabot A and Tarancón A 2018 Large-area and adaptable electrospun silicon-based thermoelectric nanomaterials with high energy conversion efficiencies *Nat. Commun.* **9** 4759
- [57] Zhang Q, He J, Zhu T J, Zhang S N, Zhao X B and Tritt T M 2008 High figures of merit and natural nanostructures in Mg₂Si_{0.4}Sn_{0.6} based thermoelectric materials *Appl. Phys. Lett.* **93** 102109
- [58] Berger H H 1972 Contact Resistance and Contact Resistivity *J. Electrochem. Soc.*
- [59] Rowe D M and Min G 1998 Evaluation of thermoelectric modules for power generation *J. Power Sources* **73** 193–8
- [60] Rowe D M and Min G 1996 Design theory of thermoelectric modules for electrical power generation *IEE Proceedings-Science, Meas. Technol.*
- [61] Mohney S E, Wang Y, Cabassi M A, Lew K K, Dey S, Redwing J M and Mayer T S 2005 Measuring the specific contact resistance of contacts to semiconductor nanowires *Solid. State. Electron.* **49** 227–32
- [62] Stavitski N, van Dal M J H, Lauwers A, Vrancken C, Kovalgin A Y and Wolters R A M 2008 Systematic TLM measurements of NiSi and PtSi specific contact resistance to n- and p-type Si in a broad doping range *IEEE Electron Device Lett.*
- [63] Chaudhry A, Ramamurthi V, Fong E and Islam M S 2007 Ultra-Low Contact Resistance of Epitaxially Interfaced Bridged Silicon Nanowires *Nano Lett.* **7** 1536–41
- [64] Sharma S, Kamins T I, Islam M S, Williams R S and Marshall A F 2005 Structural characteristics and connection mechanism of gold-catalyzed bridging silicon nanowires *J. Cryst. Growth*
- [65] Fu C J and Zhang Z M 2006 Nanoscale radiation heat transfer for silicon at different doping levels *Int. J. Heat Mass Transf.* **49** 1703–18

